

In situ Raman spectroscopy reveals the structure and dissociation of interfacial water

<https://doi.org/10.1038/s41586-021-04068-z>

Received: 7 July 2020

Accepted: 29 September 2021

Published online: 1 December 2021

 Check for updates

Yao-Hui Wang^{1,6}, Shisheng Zheng^{2,6}, Wei-Min Yang¹, Ru-Yu Zhou¹, Quan-Feng He¹, Petar Radjenovic¹, Jin-Chao Dong¹, Shunning Li², Jiaxin Zheng², Zhi-Lin Yang¹, Gary Attard³, Feng Pan^{2,✉}, Zhong-Qun Tian^{1,4} & Jian-Feng Li^{1,4,5,✉}

Understanding the structure and dynamic process of water at the solid–liquid interface is an extremely important topic in surface science, energy science and catalysis^{1–3}. As model catalysts, atomically flat single-crystal electrodes exhibit well-defined surface and electric field properties, and therefore may be used to elucidate the relationship between structure and electrocatalytic activity at the atomic level^{4,5}. Hence, studying interfacial water behaviour on single-crystal surfaces provides a framework for understanding electrocatalysis^{6,7}. However, interfacial water is notoriously difficult to probe owing to interference from bulk water and the complexity of interfacial environments⁸. Here, we use electrochemical, in situ Raman spectroscopic and computational techniques to investigate the interfacial water on atomically flat Pd single-crystal surfaces. Direct spectral evidence reveals that interfacial water consists of hydrogen-bonded and hydrated Na⁺ ion water. At hydrogen evolution reaction (HER) potentials, dynamic changes in the structure of interfacial water were observed from a random distribution to an ordered structure due to bias potential and Na⁺ ion cooperation. Structurally ordered interfacial water facilitated high-efficiency electron transfer across the interface, resulting in higher HER rates. The electrolytes and electrode surface effects on interfacial water were also probed and found to affect water structure. Therefore, through local cation tuning strategies, we anticipate that these results may be generalized to enable ordered interfacial water to improve electrocatalytic reaction rates.

The HER is a scientifically significant electrochemical reaction, as many of the fundamental laws of electrode kinetics, as well as many modern concepts in electrochemistry, were developed and verified by probing HER mechanisms related to electron-transfer-induced water dissociation^{9–11}. Furthermore, regulation of the HER rate by cations has been reported recently^{12,13}. Nevertheless, despite the fact that interfacial water is the most important player in HER, its structure and composition, and its interaction with cations in regulating the potential dependence of the HER, remain somewhat obscure and require further, more detailed understanding. To this end, a host of in situ monitoring techniques have been developed, such as vibrational spectroscopy (infrared absorption spectroscopy^{14,15} and sum-frequency generation spectroscopy^{16,17}) and X-ray spectroscopy⁸. However, these techniques typically focus on probing interfacial water at potentials close to the potential of zero charge (PZC). Thus, they lack practical application in relation to interfacial water molecules reacting on single-crystal surfaces at significant HER overpotentials, which

clearly limits our understanding of the HER under real electrolysis conditions.

Surface-enhanced Raman scattering (SERS) is a highly surface-sensitive technique that is capable of single-molecule-level resolution. However, atomically flat single-crystal surfaces cannot effectively support the surface plasmon resonance effect required for accurate detection of surface chemical speciation with SERS. The shell-isolated nanoparticle-enhanced Raman spectroscopy (SHINERS)¹⁸ technique was invented to overcome the intrinsic morphological limitation of SERS, and can be employed to study electrocatalytic reactions on single-crystal surfaces with extremely high surface sensitivity¹⁹.

Here, we investigate the structure and dissociation process of interfacial water on atomically flat Pd single-crystal (Pd(*hkl*)) surfaces by combining in situ Raman spectroscopy (SHINERS) and ab initio molecular dynamics (AIMD) simulations. Pd is one of the most extensively studied HER electrocatalysts and is the focus of this study. We elucidate the

¹State Key Laboratory of Physical Chemistry of Solid Surfaces, MOE Key Laboratory of Spectrochemical Analysis and Instrumentation, iChEM, College of Chemistry and Chemical Engineering, College of Energy, College of Materials, College of Physical Science and Technology, Xiamen University, Xiamen, China. ²School of Advanced Materials, Peking University, Shenzhen Graduate School, Shenzhen, China. ³Department of Physics, University of Liverpool, Liverpool, UK. ⁴Innovation Laboratory for Sciences and Technologies of Energy Materials of Fujian Province (IKKEM), Xiamen, China. ⁵College of Optical and Electronic Technology, China Jiliang University, Hangzhou, China. ⁶These authors contributed equally: Yao-Hui Wang, Shisheng Zheng.

✉e-mail: panfeng@pkusz.edu.cn; li@xmu.edu.cn

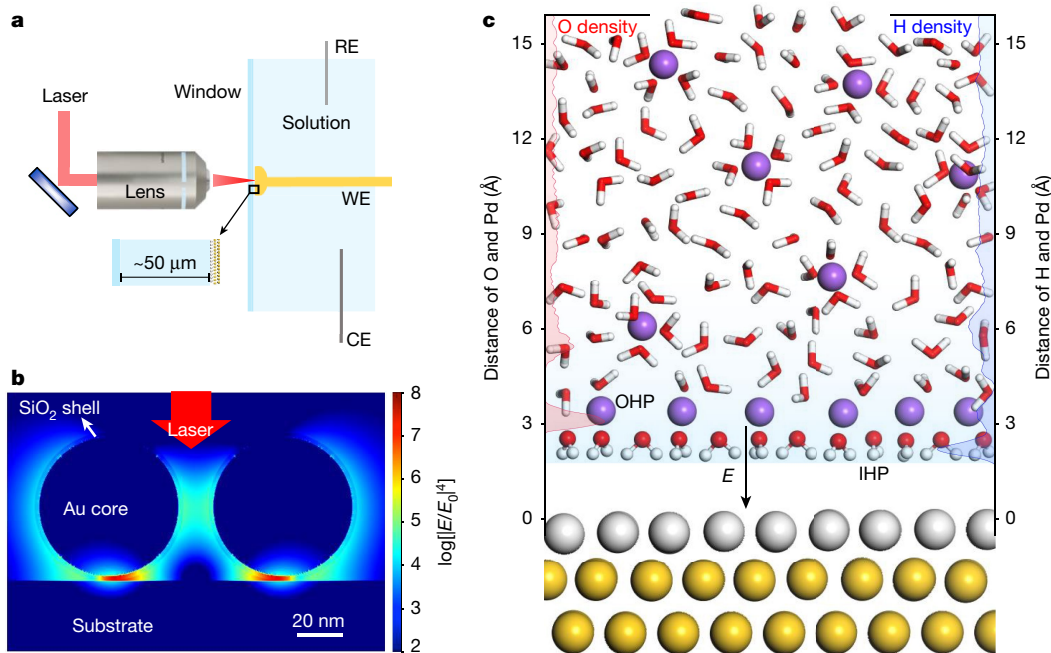


Fig. 1 | Probing interfacial water on Pd(*hkl*) surfaces. **a**, Schematic of the Raman experimental setup. CE, counter electrode; RE, reference electrode; WE, working electrode. **b**, 3D-finite-difference-time-domain (3D-FDTD) simulation of electromagnetic field distribution 2×2 array of SHINs on the

Pd/Au substrate, where E and E_0 denote the localized electric field and the incident electric field. **c**, Schematic of the interfacial model of the Pd/Au surface. Pd, Au, O, H and Na atoms are shown in silver, yellow, red, white and purple, respectively. E , electric field.

mechanism of structural ordering of interfacial water and the effect of local cation perturbation of the structure of interfacial water, and consequently the electrocatalytic reaction rate.

The three-electrode experimental system consisted of an ultra-thin ($\sim 50 \mu\text{m}$ thick) solution trapped between the working electrode surface and a quartz window to reduce the influence of bulk water (Fig. 1a).

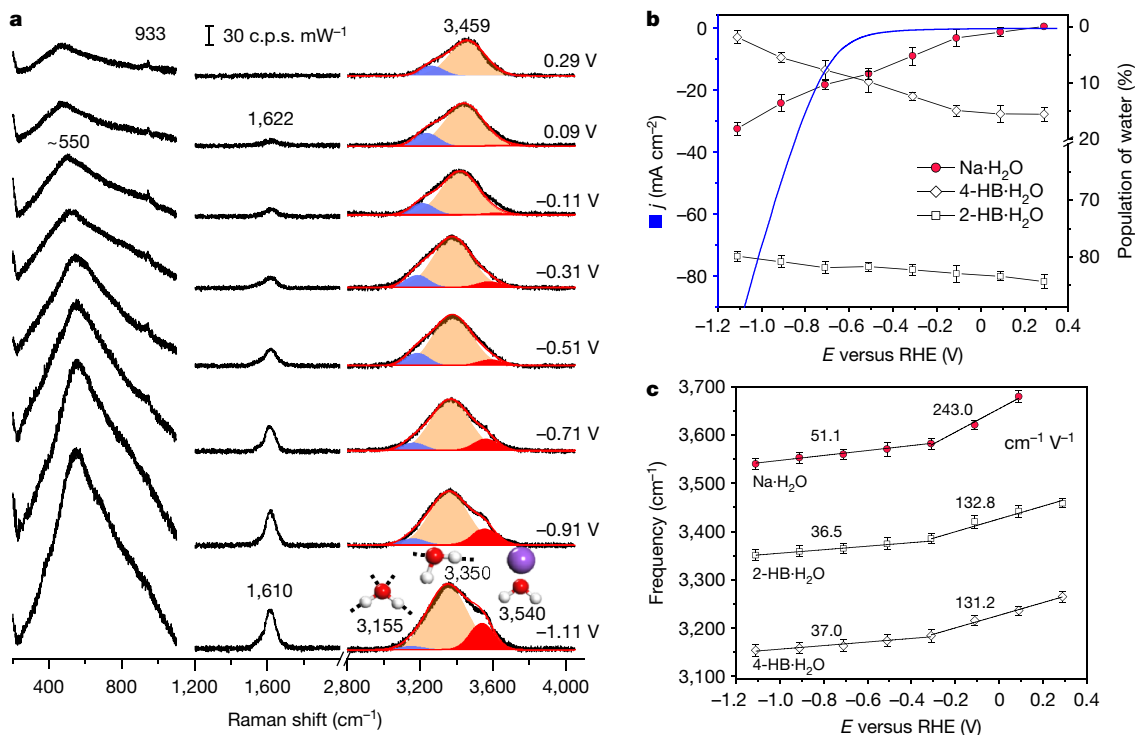


Fig. 2 | Raman spectra of interfacial water. **a**, In situ Raman spectra of interfacial water on a Pd(111) electrode in a 0.1 M NaClO₄ solution (pH 11). Gaussian fits of three O–H stretching modes are shown in blue, orange and red, respectively. c.p.s., counts per second. **b**, Potential-dependent population of interfacial water from in situ Raman spectra and HER current density (HER

current density was recorded in an electrochemical cell). **c**, Frequency plot of changes in the O–H stretching modes in Raman spectra of interfacial water. Error bars in **b** and **c** represent s.d. for each data point ($n = 3$ independent experiments), and points are average values.

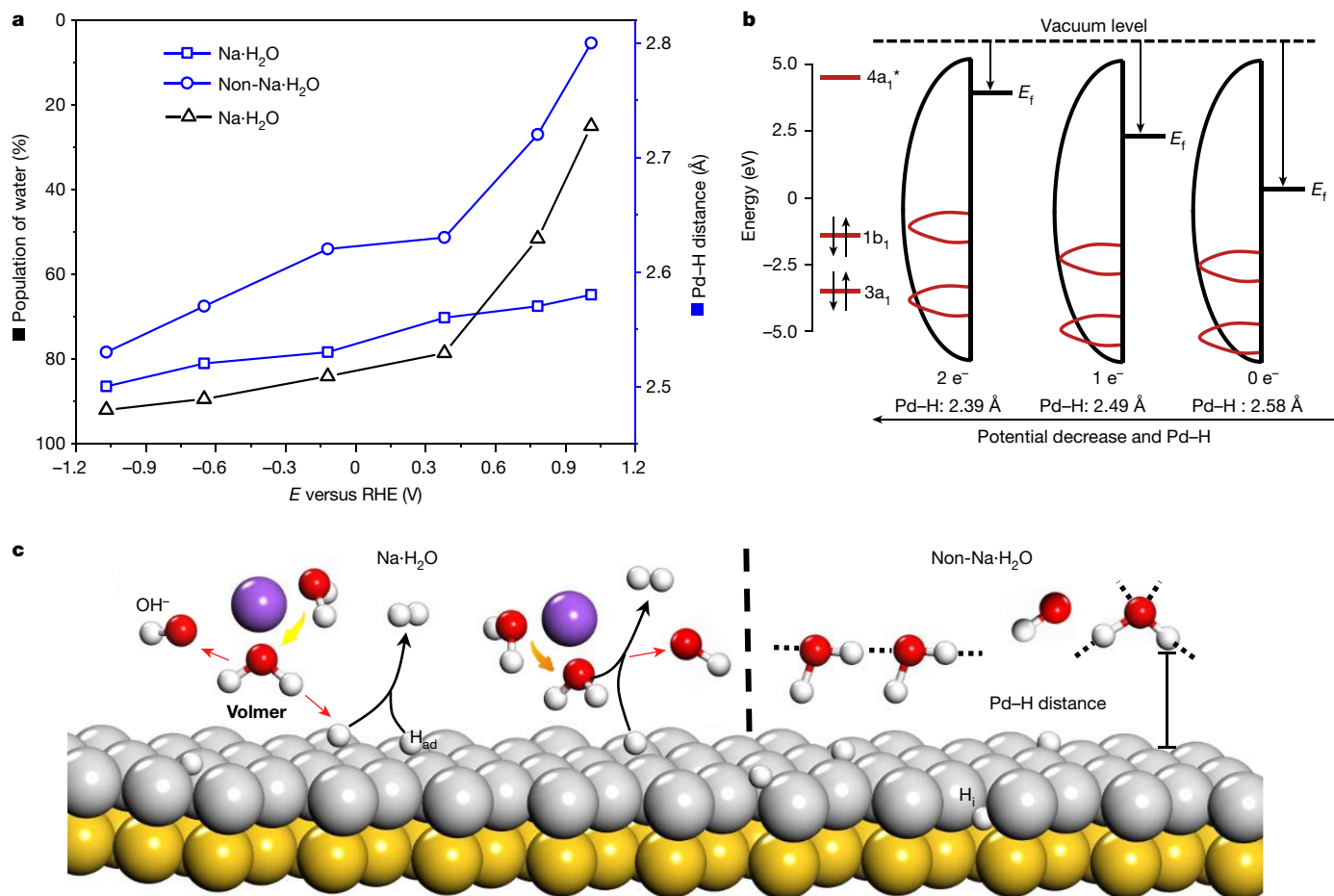


Fig. 3 | Water dissociation. **a**, From AIMD simulations, calculated Pd–H distances of Na-H₂O (blue squares) and non-Na-H₂O (blue circles), and the Na-H₂O population (black) of interfacial water at different potentials. Na-H₂O is defined as water in which the distance between the O atom and Na is less than 3.2 Å (see Supplementary Fig. 17). **b**, Schematic showing the change in

the density of states for the main orbital interactions between H₂O (red line) and the underneath Pd atom (black line) with decreasing potential using a Na-H₂O cluster model (original data are presented in Supplementary Fig. 18). **c**, Schematic showing interfacial water dissociation on a Pd(111) surface (Au(111) coated with Pd monolayer).

A vertically placed homemade electrochemical Raman cell was used to eliminate the influence of evolved hydrogen bubbles during in situ Raman measurements. Raman (SHINERS) is well suited to probing interfacial water over bulk water, as the strong signal enhancement comes from electromagnetic fields located at the junctions between shell-isolated nanoparticles (SHINs) and the substrate (Fig. 1b). Moreover, based on the Stern model (the Gouy–Chapman layer can be omitted under high ionic strength conditions), AIMD was used to simulate the atomic structure of interfacial water on Pd/Au (Pd monolayer on Au) when a bias potential is applied (Fig. 1c). The electric field was found to locate between the metal surface and electrolyte solution, including at the inner Helmholtz plane (IHP) and outer Helmholtz plane (OHP), with Na⁺ ions acting as counterions to compensate for the negatively charged electrode surface. The interfacial water molecules are defined as being within 4.0 Å of the Pd surface according to the oxygen and hydrogen density distribution (detailed in Supplementary Fig. 14).

Figure 2a shows in situ electrochemical Raman spectra of interfacial water on a Pd(111) surface in 0.1 M NaClO₄ solution (pH 11) saturated with Ar over the potential range from 0.29 V to –1.11 V (all potentials are referenced to the reversible hydrogen electrode (RHE)). At 0.29 V, two Raman bands are visible: a band at 933 cm⁻¹ from ClO₄⁻ and a broad band extending from 3,000 to 3,800 cm⁻¹ from the O–H stretching mode of H₂O (ref. 20). A new broad Raman band centered at ~550 cm⁻¹ appears at –0.11 V, attributed to the libration mode of H₂O (ref. 21), and its intensity gradually increases as the potential decreases to –1.11 V.

The intensity of the ~550 cm⁻¹ band is closely related to the orderliness of the interfacial water structure²¹. Thus, the increasing intensity of the ~550 cm⁻¹ band with decreasing potential implies that interfacial water forms a specially ordered structure²². AIMD simulations describe the dynamic restructuring processes of interfacial water from a random to a more ordered distribution, composed of a sequence of one-H-down followed by a two-H-down type interfacial water (Supplementary Fig. 15a,b). An additional band of the HOH bending mode of water at 1,622 cm⁻¹ appears at 0.09 V and then shifts to 1,610 cm⁻¹ as the potential decreases to –1.11 V, which indicates the weak hydrogen-bond interactions between interfacial water at negative potentials²³. The reduced number of hydrogen-bond donors (*N*_{donor}) at the interface at negative potential (Supplementary Fig. 15c) also indicates weak hydrogen-bond interactions.

Gaussian fitting of the spectra shows that the O–H stretching band (Fig. 2a) can be resolved into three distinct components, corresponding to three types of O–H stretching vibrations^{24,25}. The low wavenumber component (Fig. 2a, blue) and main component (Fig. 2a, orange) are associated with 4-coordinated hydrogen-bonded water (4-HB-H₂O) and 2-coordinated hydrogen-bonded water (2-HB-H₂O), respectively. The high wavenumber component (Fig. 2a, red) is attributed to Na⁺ ion hydrated water (Na-H₂O) with weak hydrogen-bond interactions, and this becomes the main interfacial water band in high concentration (8.0 M) NaClO₄ solution (Supplementary Fig. 9a). The ~550 cm⁻¹ Raman band of interfacial water at –1.11 V (Supplementary Fig. 9b) is

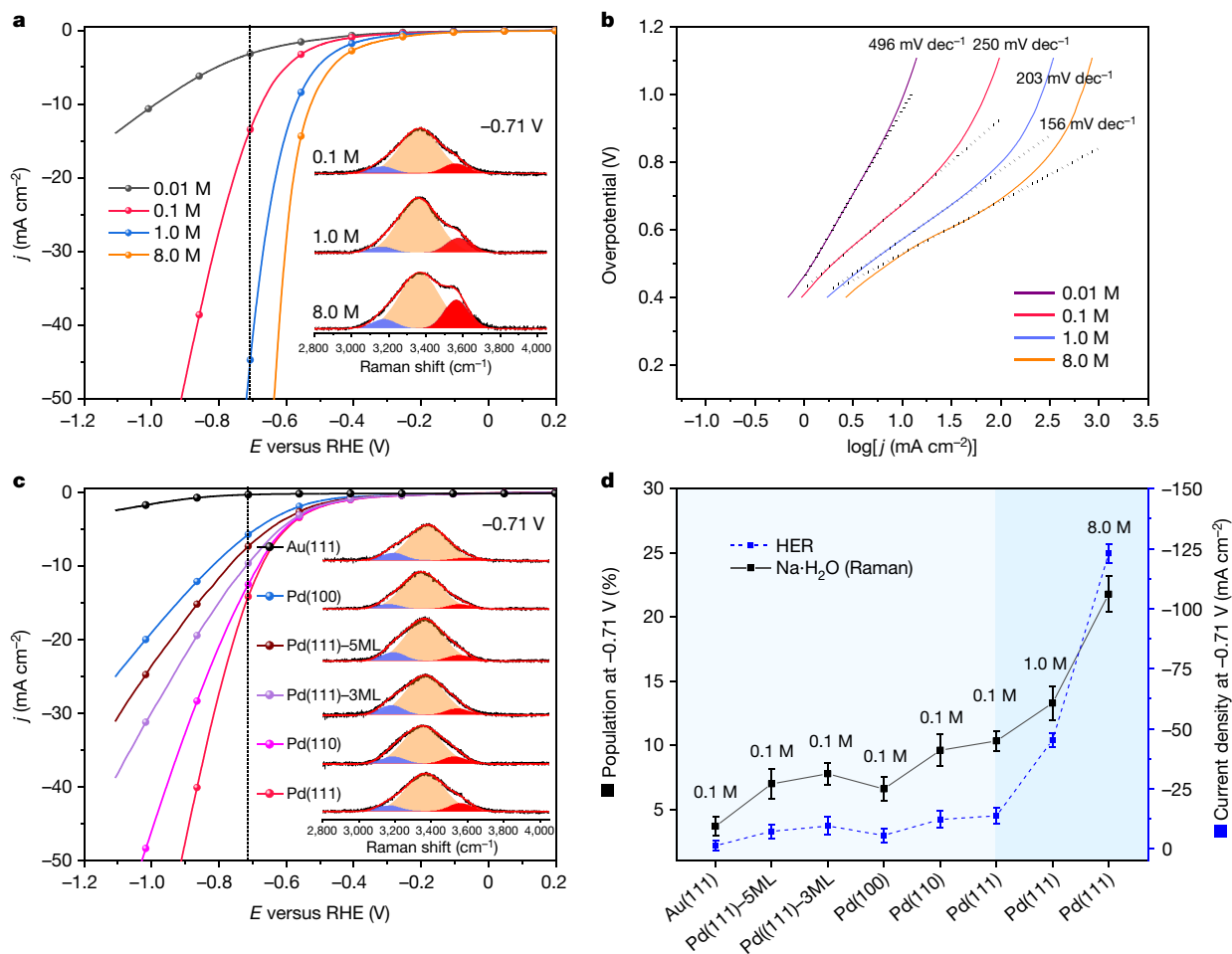


Fig. 4 | HER profiles and Raman spectra of interfacial water. **a**, HER profiles and Raman spectra of O–H stretching mode (inset). 5 mV s^{-1} scan rate and 1,600 r.p.m. **b**, Tafel slopes of the HER for Pd(111) in different concentration NaClO_4 (pH 11) solutions. **c**, HER profiles and Raman spectra of O–H stretching

much stronger at higher concentrations of NaClO_4 , indicating that $\text{Na}\cdot\text{H}_2\text{O}$ is more ordered than hydrogen-bonded water.

A better description of the three types of water populations on the Pd(111) surface can be described by comparing the proportion of O–H stretching Raman band. Analysis of the results in Fig. 2b shows that as the potential decreased, the populations of 4-HB- H_2O decreased from $15.6\% \pm 1.3\%$ (s.d.) to $2.6\% \pm 1.1\%$, 2-HB- H_2O varied between $79.1\% \pm 1.3\%$ and $84.4\% \pm 1.3\%$, and $\text{Na}\cdot\text{H}_2\text{O}$ increased from 0 to $18.3\% \pm 1.0\%$. The increase in $\text{Na}\cdot\text{H}_2\text{O}$ population on the surface is mainly caused by the electrostatic effect of the Na^+ cations migrating to the surface to charge-compensate at negative potentials. Calculations of the increased ratio of $\text{Na}\cdot\text{H}_2\text{O}$ (Fig. 3a) and increased Na^+ ion concentration (Supplementary Fig. 16) at the interface at negative potentials generally fit the experimental observations. A more ordered water structure is formed at more negative potentials as a result of the libration band ($\sim 550 \text{ cm}^{-1}$) and increased $\text{Na}\cdot\text{H}_2\text{O}$ population. Meanwhile, the HER current density increases as the potential decreases (Fig. 2b). A special relationship between the $\text{Na}\cdot\text{H}_2\text{O}$ population and the HER is deduced as they both tend to increase simultaneously.

Moreover, the vibrational frequency of adsorbate varies as a function of electrode potential and has been attributed to the vibrational Stark effect²⁶. Figure 2c shows the Stark slopes of $\text{Na}\cdot\text{H}_2\text{O}$, 2-HB- H_2O and 4-HB- H_2O . The steeper Stark slope shows that the $\text{Na}\cdot\text{H}_2\text{O}$ is more sensitive to the local electric field than 2-HB- H_2O and 4-HB- H_2O (ref. 27). According to the AIMD results pertaining to the interfacial water

mode (inset). 5 mV s^{-1} scan rate and 1,600 r.p.m. **d**, The correlations of $\text{Na}\cdot\text{H}_2\text{O}$ populations and HER current density at -0.71 V on single-crystal surfaces in NaClO_4 solution (pH 11). Error bars represent s.d. for each data point ($n = 3$ independent experiments), and points are average values.

orientation (Supplementary Fig. 15d), the structure of $\text{Na}\cdot\text{H}_2\text{O}$ is different to other water molecules in that the vibrational dipole moment of $\text{Na}\cdot\text{H}_2\text{O}$ (the direction of the OH bond) is more parallel to the direction of the electric field under all potentials, indicating that $\text{Na}\cdot\text{H}_2\text{O}$ is more likely to transform into the two-H-down structure than 2-HB- H_2O and 4-HB- H_2O .

The AIMD simulation results further show that the Pd–H distance of $\text{Na}\cdot\text{H}_2\text{O}$ is shorter than that of non- $\text{Na}\cdot\text{H}_2\text{O}$ at all potentials (Fig. 3a, blue line). A $\text{Na}\cdot\text{H}_2\text{O}$ cluster model (Supplementary Fig. 18a) was used to investigate the effect of shorter Pd–H distances in $\text{Na}\cdot\text{H}_2\text{O}$ during water dissociation. The results are shown in Fig. 3b; as the potential decreases, the Pd–H distance decreases along with the Fermi level (E_F) of Pd approaching the empty $4a_1^*$ antibonding orbital of water, which strengthens the Pd–H bonding interaction and facilitates water dissociation. Figure 3c describes the dissociation process (Volmer step) of $\text{Na}\cdot\text{H}_2\text{O}$, including adsorbed hydrogen atom (H_{ad}) formation and subsequent hydrogen generation (Tafel step or Heyrovsky step)²⁸. In this regard, the interfacial Na^+ ions serve as a ‘co-catalyst’ by continuously supplying water to the interface, as well as improving the electron transfer efficiency between the electrode and the interfacial water.

The relationship between interfacial $\text{Na}\cdot\text{H}_2\text{O}$ population and the HER performance was studied further on the Pd(111) surface (Fig. 4a,b). For the same current density of -10 mA cm^{-2} , the potential for HER shifted positively; approximately 314 mV (0.1 M), 416 mV (1.0 M) and 461 mV

(8.0 M) with respect to the 0.01 M NaClO₄ (pH 11). The HER activity notably increases as the NaClO₄ concentration increases. This trend was also verified on Au(poly) in NaClO₄ solution (pH 11), and on Pd(111) in PBS buffer solution (pH 7.2) (Supplementary Fig. 5a,d). Spectral analysis of the Raman spectra of the O–H stretching mode (inset in Fig. 4a) reveals that the interfacial Na·H₂O populations at –0.71 V are 10.6% ± 1.0%, 13.3% ± 1.3% and 21.8% ± 1.4% in 0.1 M, 1.0 M and 8.0 M NaClO₄ (pH 11, Supplementary Table 1), respectively. Figure 4b shows HER Tafel slopes of 496, 250, 203 and 156 mV dec^{–1} for 0.01 M, 0.1 M, 1.0 M and 8.0 M NaClO₄ solutions, respectively. The decreasing Tafel slope and overpotential of HER in NaClO₄ of higher concentrations indicate that the HER rate is accelerated by the ordered Na·H₂O structures. The HER performance in 0.1 M cation-varied (Li⁺, K⁺, Cs⁺, Ca²⁺, Sr²⁺, Ba²⁺) perchlorate solutions and 0.1 M NaF solution (pH 11) were also studied on Pd(111) and Au(poly) surfaces (Supplementary Fig. 5b,c). Similar cyclic voltammetry curves were observed in +1 valence cation solutions, however the HER activity increased in +2 valence cation solution, indicating that the increased HER performance is related to the ionic strength.

Next, the influence of the crystallographic orientation of interfacial water on three low-index single-crystal surfaces, (111), (100) and (110) facets, was studied. A better HER performance on Pd(111) was observed (Fig. 4c), and the population of interfacial Na·H₂O was also relatively high on Pd(111) at 10.6% ± 1.0%, compared to 9.6% ± 1.2% for Pd(110) and 6.6% ± 0.9% for Pd(100) (Fig. 4d) according to the Raman results shown in the inset of Fig. 4c. A more positive PZC on the Pd(111) surface (Supplementary PZC section) indicates a higher surface charge density. For electronic structural effects, the HER activities of different Pd layers on Au(111) single-crystal surface (Fig. 4c) decreased in the order Pd(111) > Pd(111)–3ML > Pd(111)–5ML. Meanwhile, the population of interfacial Na·H₂O on Pd(111) (10.6% ± 1.0%) is also higher than on Pd(111)–3ML (7.8% ± 0.8%) and Pd(111)–5ML (7.0% ± 1.2%) (Fig. 4d). The suppressed atomic hydrogen (H₁, Fig. 3c) in the Pd bulk lattice²⁹ and the more positive PZC on Pd(111) than on Pd(111)–3ML and Pd(111)–5ML accounts for the higher HER activity. In summary, a higher Na·H₂O population and better HER performance on Pd(111) indicates high-efficiency electron transference between water and the electrode at the interface. Therefore, we propose that the ordered Na·H₂O structure (which is attributed to Na⁺ ions ‘tuning’ the degree of ordering in water overall at negative electrode charges) boosts HER activity.

Here, we have developed a framework to correlate the cations and the structure of interfacial water with the electrocatalytic performance of a HER electrocatalyst. Under bias potential, hydrated cations bonded to water molecules are guided towards the Pd surface to reduce the Pd–H distance and promote the charge transfer efficiency to enhance the HER performance, which is also directly proportional to the concentration and ionic strength of cations owing to the effect of interface electrostatic interaction. From the perspective of thermodynamics, through local hydrated cation tuning strategies in the vicinity of the interface, disordered bulk H₂O can be effectively arranged into ordered interfacial H₂O (that is, an entropy decrease process) in a finite region to minimize additional work and to maximize electrochemistry energy conversion. In this regard, co-catalyst interfacial cations alter the transmission route of reactants and products in the HER, resulting in improved reaction rates. The findings and experimental capability established here raise the exciting prospect of future work following the onset of interfacial water structure in aqueous electrocatalytic reactions and hence the use of cation tuning strategies in other energy conversion fields.

Online content

Any methods, additional references, Nature Research reporting summaries, source data, extended data, supplementary information, acknowledgements, peer review information; details of author contributions and competing interests; and statements of data and code availability are available at <https://doi.org/10.1038/s41586-021-04068-z>.

- Seh, Z. W. et al. Combining theory and experiment in electrocatalysis: insights into materials design. *Science* **355**, eaad4998 (2017).
- Mubeen, S. et al. An autonomous photosynthetic device in which all charge carriers derive from surface plasmons. *Nat. Nanotechnol.* **8**, 247–251 (2013).
- Guo, J. et al. Real-space imaging of interfacial water with submolecular resolution. *Nat. Mater.* **13**, 184–189 (2014).
- Vidal-Iglesias, F. J., Solla-Gullon, J., Herrero, E., Aldaz, A. & Feliu, J. M. Pd adatom decorated (100) preferentially oriented Pt nanoparticles for formic acid electrooxidation. *Angew. Chem. Int. Ed.* **49**, 6998–7001 (2010).
- Strmcnik, D. et al. Enhanced electrocatalysis of the oxygen reduction reaction based on patterning of platinum surfaces with cyanide. *Nat. Chem.* **2**, 880–885 (2010).
- Kendrick, E., Kendrick, J., Knight, K. S., Islam, M. S. & Slater, P. R. Cooperative mechanisms of fast-ion conduction in gallium-based oxides with tetrahedral moieties. *Nat. Mater.* **6**, 871–875 (2007).
- Mesa, C. A. et al. Multihole water oxidation catalysis on haematite photoanodes revealed by operando spectroelectrochemistry and DFT. *Nat. Chem.* **12**, 82–89 (2020).
- Velasco-Velez, J. J. et al. The structure of interfacial water on gold electrodes studied by x-ray absorption spectroscopy. *Science* **346**, 831–834 (2014).
- Subbaraman, R. et al. Trends in activity for the water electrolyser reactions on 3d M(Ni,Co,Fe,Mn) hydr(oxy)oxide catalysts. *Nat. Mater.* **11**, 550–557 (2012).
- Wang, X., Xu, C., Jaroniec, M., Zheng, Y. & Qiao, S. Z. Anomalous hydrogen evolution behavior in high-pH environment induced by locally generated hydronium ions. *Nat. Commun.* **10**, 4876 (2019).
- Ledezma-Yanez, I. et al. Interfacial water reorganization as a pH-dependent descriptor of the hydrogen evolution rate on platinum electrodes. *Nat. Energy* **2**, 17031 (2017).
- Guha, A., Narayanan, S. & Narayanan, T. N. Tuning the hydrogen evolution reaction on metals by lithium salt. *ACS Appl. Energy Mater.* **1**, 7116–7122 (2018).
- Guha, A., Kaley, N. M., Mondal, J. & Narayanan, T. N. Engineering the hydrogen evolution reaction of transition metals: effect of Li ions. *J. Mater. Chem. A* **8**, 15795–15808 (2020).
- Ataka, K., Yotsuyanagi, T. & Osawa, M. Potential-dependent reorientation of water molecules at an electrode/electrolyte interface studied by surface-enhanced infrared absorption spectroscopy. *J. Phys. Chem.* **100**, 10664–10672, (1996).
- Yamakata, A. & Osawa, M. Destruction of the hydration shell around tetraalkylammonium ions at the electrochemical interface. *J. Am. Chem. Soc.* **131**, 6892–6893, (2009).
- Tong, Y., Lapointe, F., Thamer, M., Wolf, M. & Campen, R. K. Hydrophobic water probed experimentally at the gold electrode/aqueous interface. *Angew. Chem. Int. Ed.* **56**, 4211–4214 (2017).
- Liu, W. T. & Shen, Y. R. In situ sum-frequency vibrational spectroscopy of electrochemical interfaces with surface plasmon resonance. *Proc. Natl Acad. Sci. USA* **111**, 1293–1297 (2014).
- Li, J. F. et al. Shell-isolated nanoparticle-enhanced Raman spectroscopy. *Nature* **464**, 392–395 (2010).
- Dong, J. C. et al. In situ Raman spectroscopic evidence for oxygen reduction reaction intermediates at platinum single-crystal surfaces. *Nat. Energy* **4**, 60–67 (2019).
- Davis, J. G., Gierszal, K. P., Wang, P. & Ben-Amotz, D. Water structural transformation at molecular hydrophobic interfaces. *Nature* **491**, 582–585 (2012).
- Chen, Y. X., Zou, S. Z., Huang, K. Q. & Tian, Z. Q. SERS studies of electrode/electrolyte interfacial water part II—librations of water correlated to hydrogen evolution reaction. *J. Raman Spectrosc.* **29**, 749–756 (1998).
- Toney, M. F. et al. Voltage-dependent ordering of water molecules at an electrode-electrolyte interface. *Nature* **368**, 444–446 (1994).
- Senior, W. A. & Thompson, W. K. Assignment of the infra-red and Raman bands of liquid water. *Nature* **205**, 170 (1965).
- Chen, H. C. et al. Active and stable liquid water innovatively prepared using resonantly illuminated gold nanoparticles. *ACS Nano* **8**, 2704–2713 (2014).
- Scatena, L. F., Brown, M. G. & Richmond, G. L. Water at hydrophobic surfaces: weak hydrogen bonding and strong orientation effects. *Science* **292**, 908–912 (2001).
- Lambert, D. K. Vibrational Stark effect of adsorbates at electrochemical interfaces. *Electrochim. Acta* **41**, 623–630 (1996).
- Li, J. F. et al. SERS and DFT study of water on metal cathodes of silver, gold and platinum nanoparticles. *Phys. Chem. Chem. Phys.* **12**, 2493–2502 (2010).
- Subbaraman, R. et al. Enhancing hydrogen evolution activity in water splitting by tailoring Li⁺-Ni(OH)₂-Pt interfaces. *Science* **334**, 1256–1260 (2011).
- Kibler, L. A. Hydrogen electrocatalysis. *ChemPhysChem* **7**, 985–991 (2006).

Publisher's note Springer Nature remains neutral with regard to jurisdictional claims in published maps and institutional affiliations.

© The Author(s), under exclusive licence to Springer Nature Limited 2021

Methods

Electrochemical measurement

All single-crystal electrochemical experiments were carried out in a hanging meniscus configuration with a CHI760E bipotentiostat (CH Instruments) and a homemade glass three-electrode cell, using Pt wire (or graphite rod for HER measurements) as the counter electrode, and a home-made RHE or saturated calomel electrode (SCE) (KCl sat.) as the reference electrode. The HER measurements were carried out in a hanging meniscus rotating disk electrode configuration system. Unless stated otherwise, all potentials were referenced to the RHE, and all HER polarization curves were current-resistance (iR) corrected. After calibration, all of the polarization data were presented with respect to the electrode surface area. All solutions for electrochemical measurements were deaerated by Ar and a flow of Ar was maintained over all of the electrochemical tests. The pH value of the NaClO₄ solution was adjusted by means of a NaOH solution.

In situ Raman experimental setup

The electrochemical Raman measurements were carried out on a confocal microscope Raman system, including EC-Raman (Xiamen SHINS Technology) and XploRA (HORIBA). A He-Ne laser with 637.8 nm excitation wavelength and a 50× microscope objective with a numerical aperture of 0.55 were used in all measurements. Raman frequency was calibrated by a Si wafer during each experiment. In situ electrochemical Raman experiments were employed in a homemade Raman cell and an Autolab PGSTAT30 (Metrohm) potentiostat was used to control the potential.

AIMD method

The calculations were performed by means of density functional theory (DFT) using Vienna ab initio simulation pack (VASP) with the projector augmented wave (PAW)³⁰ method. A plane-wave cutoff energy of 420 eV was adopted and the revised Perdew–Burke–Ernzerhof (RPBE)^{31–33} exchange–correlation functional was employed. Dispersion effects have been considered within the semi-empirical D3 (ref.³⁴) van der Waals corrections. The properties of Pd(111) water models are derived from AIMD simulations with a time step of 0.5 fs, and canonical ensemble (NVT) conditions were imposed by a Nose–Hoover thermostat with a target temperature of 330 K. For all of the molecular dynamics trajectories, the initial ~3 ps (6,000 steps) was treated as the equilibration period, and the statistical sampling was performed during the following

~7 ps (14,000 steps). Owing to the large size of the supercells, only Γ point was employed.

Data availability

The data generated or analysed during this study are included in this published article and its Supplementary information files. Source data are provided with this paper.

Code availability

The code that supports the findings of this research is available from the corresponding authors upon reasonable request.

30. Kresse, G. & Joubert, D. From ultrasoft pseudopotentials to the projector augmented-wave method. *Phys. Rev. B* **59**, 1758–1775 (1999).
31. Hammer, B., Hansen, L. B. & Nørskov, J. K. Improved adsorption energetics within density-functional theory using revised Perdew–Burke–Ernzerhof functionals. *Phys. Rev. B* **59**, 7413–7421 (1999).
32. Tonigold, K. & Gross, A. Dispersive interactions in water bilayers at metallic surfaces: a comparison of the PBE and RPBE functional including semiempirical dispersion corrections. *J. Comput. Chem.* **33**, 695–701 (2012).
33. Sakong, S., Forster-Tonigold, K. & Gross, A. The structure of water at a Pt(111) electrode and the potential of zero charge studied from first principles. *J. Chem. Phys.* **144**, 194701 (2016).
34. Grimme, S., Antony, J., Ehrlich, S. & Krieg, H. A consistent and accurate ab initio parametrization of density functional dispersion correction (DFT-D) for the 94 elements H–Pu. *J. Chem. Phys.* **132**, 154104 (2010).

Acknowledgements This work was financially supported by the National Key Research and Development Program of China (2019YFA0705400, 2020YFB1505800, 2020YFB0704500 and 2019YFD0901100), the National Natural Science Foundation of China (21925404, 22021001, 21521004, 21775127, 21991151 and 21902137), the Shenzhen Science and Technology Research Grant (JCYJ20200109140416788) and ‘111’ Project (B17027). We thank Y. X. Chen, B. W. Mao, D. P. Zhan, Z. Wei and J. B. Le for fruitful discussions, and Q. Q. Zhao, M. F. Cao and Y. Hui for technical assistance.

Author contributions Y.-H.W., S.Z., F.P. and J.-F.L. conceived the project; Y.-H.W., R.-Y.Z. and Q.-F.H. conducted the experiments; F.P., S.Z., S.L. and J.Z. performed the mechanism study and AIMD simulation; W.-M.Y. and Z.-L.Y. performed the 3D-FDTD simulation; Y.-H.W., S.Z., P.R., G.A., F.P., Z.-Q.T. and J.-F.L. wrote the paper. All authors participated in the analysis and discussion.

Competing interests The authors declare no competing interests.

Additional information

Supplementary information The online version contains supplementary material available at <https://doi.org/10.1038/s41586-021-04068-z>.

Correspondence and requests for materials should be addressed to Feng Pan or Jian-Feng Li.

Peer review information Nature thanks Angel Cuesta and the other, anonymous, reviewer(s) for their contribution to the peer review of this work.

Reprints and permissions information is available at <http://www.nature.com/reprints>.